Fast 4D tensile test monitored via X-CT: Single projection based Digital Volume Correlation dedicated to slender samples

Clément Jailin, Ante Buljac, Amine Bouterf, François Hild, Stephane Roux

Fast 4D tensile test monitored via X-CT: Single projection based Digital Volume Correlation dedicated to slender samples

Clément Jailin[1], Ante Buljac[1,2], Amine Bouterf[1], François Hild[1], Stéphane Roux[1]

[1] LMT (ENS Paris-Saclay/CNRS/Univ. Paris-Saclay)
61 avenue du Président Wilson, 94235 Cachan (FRANCE)
[2] MINES ParisTech, PSL Research University,
Centre des Matériaux, CNRS UMR 7633, BP 87, 91003 Evry (FRANCE)

Abstract

The measurement of 4D (*i.e.,* 3D space and time) displacement fields of *in situ* tests within X-ray Computed Tomography scanners (i.e., lab-scale X-CT) is considered herein using projection-based Digital Volume Correlation. With one *single* projection per loading (i.e. time) step, the developed method allows for loading not to be interrupted and to vary continuously during the scan rotation. As a result, huge gains in acquisition time (*i.e.,* more than two orders of magnitudes) to be reached. The kinematic analysis is carried out using predefined space and time bases combined with model reduction techniques (*i.e.,* Proper Generalized Decomposition with space-time decomposition). The accuracy of the measured kinematic basis is assessed via gray level residual fields. An application to an *in situ* tensile test composed of 127 time steps is performed. Because of the slender geometry of the sample, a specific beam space regularization is used, which is composed of a stack of rigid sections. Large improvements on the residual, whose SNR evolves from 9.9 dB to 26.7 dB, validate the procedure.

Keywords: 4D measurements; Digital Volume Correlation; *In situ* test; Model reduction; Tomography

1 Introduction

The development of Computed Tomography (CT) has been a major breakthrough in materials science [1, 2, 3, 4], providing nondestructive measurements of the 3D microstructure of imaged samples. Initially developed using synchrotron sources, it is now a common equipment accessible in laboratories. In addition to the broad range of spatial resolutions (from nanometer to few meter scans), significant progress has been achieved in ultra-fast X-ray tomography as illustrated with the 20 Hz full scan acquisition for the study of crack propagation [5].

Coupled with mechanical tests, these acquisitions become an attractive tool in experimental mechanics. First used for *ex situ* tests where the materials are deformed outside of the tomograph [6], the recent evolution of testing machines and CT makes *in situ* tests possible [7, 8, 9]. In the latter cases, the sample is imaged inside a tomograph, either with interrupted mechanical load or with a continuously evolving loading and *on-the-fly* acquisitions. Visualization of fast transformation, crack opening, or unsteady behavior become accessible. Combined with full-field measurements, *in situ* tests coupled with X-ray CT offer a quantitative basis for identifying a broad range of mechanical behavior.

A robust and accurate method to quantitatively measure kinematic data from the acquired images is Digital Image Correlation (DIC) in 2D and its 3D extension, Digital Volume Correlation (DVC). The latter aims at capturing the way a solid deforms between two states from the analysis of the corresponding 3D images. The measured displacement field is then used to calibrate model parameters from inverse problem procedures (*e.g.,* finite element model updating [10], virtual fields method [11]). The more numerous the acquisitions, the more accurate and sensitive the identification procedure. DVC methods have hence been developed in a 4D space-time framework [12, 13, 14] using all available volumes globally. In 4D analyses, an acquisition of 5 to 15 steps is usually performed.

However, the major limitation of CT imaging, especially in lab-tomographs is the acquisition time. To give orders of magnitude, each reconstructed CT volume, being composed of about one thousand 2D radiographs, takes approximately one hour to be acquired. This duration limits the number of possible acquired scans and hence restricts such identifications to time-independent behavior. Moreover, spurious motions may occur during acquisitions, blur the projections and reconstructions. In some cases it is required to wait 0.5 to 1 hour for relaxation or creep stabilization at each loading step, before each scan [15, 16].

The recently developed Projection-based DVC (P-DVC) [17] is an interesting method to circumvent these difficulties. Instead of working with a series of 3D volumes, it is proposed to directly measure the 3D displacement field from few of those radiographs. This procedure exploits the property that two projections at a given orientation of the sample under different loads contain a partial information about the full 3D kinematics, and sampling few angles may be sufficient to extract the entire displacement field. In a similar spirit, and very recently, the 3D tracking of rigid grains was proposed using few radiographs [18]. Previous works have developed the P-DVC method for the analysis of a cracked cast iron sample imaged with a synchrotron X-ray source [19, 20]. It was shown that the measurement was possible with only two orthogonal projection angles, thereby allowing for a huge gain in acquisition time (*i.e.,* a factor 300). In Ref. [21], a spatiotemporal framework was proposed in order to analyze the kinematics with a single projection per angle, provided a suited temporal regularization was used. This methodology was applied to a lab-tomograph *in situ* experiment where crack propagation in plaster was monitored and quantified (via double cleavage drilled compression test).

In order to deal with space and time displacement field, a Proper Generalized Decomposition (PGD) framework [22, 23, 24] will be used. The displacement field is decomposed over a basis of separated functions, namely, spatial modes and time (or projection angle)

modes. The spirit of the approach, which is inspired from the PGD technique, consists of a progressive enrichment of the space-time modes for displacement corrections. Modes are progressively added until a convergence criterion based on the residual field is reached. First introduced in DIC and DVC [25, 26] to provide a reduced basis for the displacement field (separating different spatial directions), PGD has been extended to the P-DVC framework for the calibration of material parameters in a lab-tomograph using a single projection instead of two [27]. In that work, deviations from a perfect rotation were taken into account over one scan in order to reach a good quality tomographic reconstruction. The spurious motions were described as small amplitude rigid body motions over time in addition to the ideally expected rotation. In the same spirit, a developed projection-based approach allows the imbibition process to be followed in sandstone at a frequency of 5 Hz using Neutron tomography [28].

In the sequel it is proposed to measure 4D (space and time) displacement fields based on a series of projections acquired at different angles. Using only one projection per angle allows the sample to be loaded and continuously rotated without hold and/or dwell time. This reduction in the number of radiographs, which is offered by the mathematical formulation, together with the now tolerable continuous loading leads to *half* the acquisition time of the previous method. The analysis of a complex kinematics, up to localization, with such an approach is a novelty.

In Section 2, a highly regularized PGD framework coupled with a P-DVC procedure is introduced in order to capture the kinematics of the studied sample. Section 3 focuses on the specific formulation of the approach to slender samples, and the space and time bases are discussed. Section 4 is devoted to the analysis of a tensile *in situ* test on nodular graphite cast iron with the proposed methodology. The experiment, which is composed of 127 time steps, is performed in 6 minutes with a continuous loading until failure. The measurement of the displacement field for each time step is presented and shown to provide very low registration residuals. A gain in acquisition time of more than two orders of magnitude compared with standard methods is obtained.

2 Full-field measurement

2.1 Projection-based DVC

The proposed approach to fast 4D (space and time) measurements is called Projection-based Digital Volume Correlation (P-DVC) [17, 20]. Instead of working with reconstructed volumes as in standard DVC (whose acquisition time is one of the major limitations of CT in laboratory facilities [29]), it aims to measure the 4D displacement field from a series of 2D projections acquired at different angles $\theta(t)$ and loadings.

The registration operation consists of minimizing the sum of squared differences between N_θ 2D projections $g(\boldsymbol{r}, t)$ of the deformed configuration at different times t, or angles $\theta(t)$ and loading steps. The procedure makes use of the 3D reference image, $F(\boldsymbol{x})$, which is reconstructed using classical means. It provides for all voxels of the 3D space $\boldsymbol{x} = (x, y, z)$

the local X-ray absorption coefficient. This reference volume, corrected by the displacement, $\boldsymbol{u}(\boldsymbol{x},t)$, and projected with the orientation $\theta(t)$ should coincide with the acquired projections, $g(\boldsymbol{r},t)$ when the displacement, $\boldsymbol{u}(\boldsymbol{x},t)$, is correctly measured. In other words, introducing the reference volume deformed by any trial displacement field, $\boldsymbol{v}$,

$$\widetilde{F}_{\boldsymbol{v}}(\boldsymbol{x}) \equiv F(\boldsymbol{x}-\boldsymbol{v}(\boldsymbol{x},t)) \tag{1}$$

and the so-called *residual field*, $\rho(\boldsymbol{r},t;\boldsymbol{v})$,

$$\rho(\boldsymbol{r},t;\boldsymbol{v}) = \Big(\Pi_{\theta(t)}[\widetilde{F}_{\boldsymbol{v}}]\Big)(\boldsymbol{r},t) - g(\boldsymbol{r},t) \tag{2}$$

the 3D displacement field, $\boldsymbol{u}(\boldsymbol{x},t)$, is sought as the minimizer of the following cost function

$$\chi^2[\boldsymbol{v}] = \sum_{\boldsymbol{r},t} \rho(\boldsymbol{r},t;\boldsymbol{v})^2 \tag{3}$$

where $\Pi_{\theta(t)}$ is the projection operator in the $\theta(t)$ angular direction, and $\boldsymbol{r}=(r,z)$ the coordinates in detector space. The integrand of the previous functional can be linearized considering small displacement field corrections $\boldsymbol{\delta u}$ compared to the microstructure correlation length

$$\chi^2[\boldsymbol{u}+\boldsymbol{\delta u}] = \sum_{\boldsymbol{r},t} \Big(\rho(\boldsymbol{r},t;\boldsymbol{u}) - \Big(\Pi_{\theta(t)}[\boldsymbol{\delta u}\cdot\boldsymbol{\nabla}\widetilde{F}_{\boldsymbol{u}}]\Big)(\boldsymbol{r},t)\Big)^2 \tag{4}$$

with $\boldsymbol{\nabla}$ the 3D gradient operator. It is noteworthy that after each evaluation of the displacement corrections $\boldsymbol{\delta u}$ from a known displacement $\boldsymbol{u}^{(n-1)}$ such that $\boldsymbol{u}^{(n)} = \boldsymbol{u}^{(n-1)} + \boldsymbol{\delta u}$, a correction of the volume $\widetilde{F}_{\boldsymbol{u}}(\boldsymbol{x})$ is performed so that the previous equation is used without approximation. The P-DVC framework requires the acquisition of one reference volume in order to compute the correction terms. The latter is to be performed ideally in the same conditions as for the experiment, but without load (or with a very modest one). This only one classical tomographic scan is generally not challenging.

In order to validate the proper evaluation of the displacement, one should consider the magnitude of the *residual* field that highlights all projection differences that are not captured by the measured displacement field (*e.g.,* noise, artifacts of the detector, ill-convergence, model error). Ideally, it should be statistically indistinguishable from noise. The Signal to Noise Ratio (SNR) can also be defined to evaluate the residual quantitatively. The higher the SNR, the better the solution. It is commonly defined as 20 times the decimal logarithm of the ratio of the standard deviation of the projections over that of the residual fields [30].

2.2 Regularization procedure

CT images are defined by a huge number of data (usually billions of voxels treated independently). However even if the displacement field is to be defined for all voxels, its regularity legitimates the use of much less degrees of freedom so that it is sought in a vector space generated by a reduced kinematic basis. In the following, it is proposed to

choose as reduced basis the product of separated space $\boldsymbol{\Phi}_j(\boldsymbol{x})$ and time $\sigma_i(t)$ fields for which the sought amplitudes are u_{ij}

$$\boldsymbol{u}(\boldsymbol{x},t) = \sum_{i=1}^{N_t}\sum_{j=1}^{N_s} u_{ij}\sigma_i(t)\boldsymbol{\Phi}_j(\boldsymbol{x}) \tag{5}$$

with the space and time dimensionality respectively N_s and N_t. Such separated expression is standard practice and implies no restrictions (provided $N_m = N_s \times N_t$ is large enough), but it will reveal convenient for the following model reduction technique. The previous displacement is written in a different way

$$\boldsymbol{u}(\boldsymbol{x},t) = \sum_{l=1}^{N_m}\left(\sum_{i=1}^{N_t} a_i^l\sigma_i(t)\right)\left(\sum_{j=1}^{N_s} b_j^l\boldsymbol{\Phi}_j(\boldsymbol{x})\right) \tag{6}$$

Hence the previous amplitude matrix is $u_{ij} = \sum_l a_i^l b_j^l$.

Different regularization procedures of the displacement field have been introduced in the literature for global DVC when the kinematics is discretized over finite element meshes [31]. Spatially, local (elastic) equilibrium-gap penalty was proposed [32, 33, 34]. Other model-based regularizations can be used to calibrate model parameters [35, 13, 14, 29]. These regularizations lead to drastic reductions in the number of unknowns and enable for seamless experimental/numerical interfaces. They will not be considered herein. A more generic approach will be followed hereafter.

2.3 Greedy approach to P-DVC

The entire problem composed of a large number of unknowns (*i.e.,* 630 degrees of freedom in the present application) may be costly. The method proposed to solve the minimization problem is the Proper Generalized Decomposition (PGD) approach, where modes are successively determined and added as long as the residual level is considered too high to be explained by noise, which corresponds to detector artifacts or if the noise is assumed to be white and Gaussian: $\chi[\boldsymbol{u}] > 2\gamma_f N_{\text{pix}}$, with γ_f the standard deviation of the noise and N_{pix} the total number of pixels on which the procedure is applied).

Proper Generalized Decomposition techniques [22, 36, 23, 24] consist of successive enrichments of the displacement field $\boldsymbol{u}(\boldsymbol{x},t)$ adding a new contribution at each iteration, each term of the sum being sought *a priori* in a separate representation. PGD-DIC and PGD-DVC [25, 26] with one-dimensional space functions are here extended to 3D space and time (*i.e.,* 4D) analyses.

In the following progressive PGD procedure, the time and spatial modes are identified successively, one per iteration, with a greedy approach [37]

$$\boldsymbol{u}^l(\boldsymbol{x},t) = \boldsymbol{u}^{l-1}(\boldsymbol{x},t) + \left(\sum_{i=1}^{N_n} a_i^l\sigma_i(t)\right)\left(\sum_{j=1}^{N_s} b_j^l\boldsymbol{\Phi}_j(\boldsymbol{x})\right) \tag{7}$$

Let us note that only the product $a_n^l b_j^l$ matters so that a convention such that $\|\{\boldsymbol{a}^l\}\| = 1$ or $\|\{\boldsymbol{b}^l\}\| = 1$ can be freely chosen without consequences. A fixed point algorithm is used to get the solution. Alternate minimizations of the two unknown column vectors $\{\boldsymbol{a}^l\}$ and $\{\boldsymbol{b}^l\}$ are proposed. The minimization of the functional leads to the determination of the unknowns with two coupled equations

$$\{\boldsymbol{a}^l\} = \underset{\{\boldsymbol{a}\}}{\text{Argmin}}(\chi^2_{\boldsymbol{u}}(\{\boldsymbol{a}\}, \{\boldsymbol{b}\})) \tag{8}$$

$$\{\boldsymbol{b}^l\} = \underset{\{\boldsymbol{b}\}}{\text{Argmin}}(\chi^2_{\boldsymbol{u}}(\{\boldsymbol{a}\}, \{\boldsymbol{b}\})) \tag{9}$$

i.e., the minimization of $\chi^2_{\boldsymbol{u}}$ with respect to the additional mode is considered.

It is proposed to write the projected sensitivity for each degree of freedom of each section as

$$S_i(\boldsymbol{r}, t) = \Pi_{\theta(t)}[\boldsymbol{\Phi}_i(\boldsymbol{x}') \cdot \boldsymbol{\nabla} F(\boldsymbol{x}')] \tag{10}$$

and the associated matrix

$$B_{ij}(t) = \sum_{\boldsymbol{r}} \boldsymbol{S}_i(\boldsymbol{r}, t) \boldsymbol{S}_j(\boldsymbol{r}, t) \tag{11}$$

where $\boldsymbol{x}'$ is the corrected position of any voxel $\boldsymbol{x}$ with the previously identified modes such that $\boldsymbol{x}' = \boldsymbol{x} - \boldsymbol{u}^{(l-1)}$. The sensitivity $S_i(\boldsymbol{r}, t)$ is composed of degrees of freedom i, pixels of the detector $\boldsymbol{r}$ and angles $\theta(t)$ hence it is of size $[N_s \times N_p \times N_\theta]$. Computing and storing this matrix is the longest operation in the procedure. The other quantities are easily obtained from combinations of these projected 3D sensitivity fields. It can be noted that $S_i(\boldsymbol{r}, t)$ should be recomputed for each identified mode while $\boldsymbol{x}'$ is updated. Because the degrees of freedom per sections are quite independent, the sensitivity matrix can be stored as a sparse matrix (and could be highly parallelized if the beam is non-diverging).

The two parts are obtained from the above linearized integrand using Newton's scheme. The derivative with respect to $\{\boldsymbol{b}^l\}$ leads to

$$\{\boldsymbol{b}^l\} = [\boldsymbol{N}^l]^{-1}\{\boldsymbol{n}^l\} \tag{12}$$

where $[\boldsymbol{N}^l]$ is the spatial Hessian matrix of $\chi^2_{\boldsymbol{u}}$ with respect to $\{\boldsymbol{b}^l\}$ (*i.e.,* $N^l_{ij} = \partial_{b_i}\partial_{b_j}\chi^2_{\boldsymbol{u}}$) and $\{\boldsymbol{n}^l\}$ the second member vector based on the residual field, which is written as a weighted sum over time of the sensitivities with $\alpha^l(t) = \sum_{i=1}^{N_n} a_i^l \sigma_i(t)$

$$N^l_{ij} = \sum_t \alpha^l(t) B_{ij}(t) \alpha^l(t) \tag{13}$$

and

$$n^l_j = \sum_{\boldsymbol{r},t} \rho(\boldsymbol{r}, t, \boldsymbol{u}^{l-1}) \alpha^l(t) S_j(\boldsymbol{r}, t) \tag{14}$$

Similarly, the derivative with respect to $\{\boldsymbol{a}^l\}$ leads to

$$\{\boldsymbol{a}^l\} = [\boldsymbol{M}]^{-1}\{\boldsymbol{m}\} \tag{15}$$

where, as previously, $[\boldsymbol{M}^l]$ is the temporal Hessian matrix (*i.e.,* $M^l_{ij} = \partial_{a_i}\partial_{a_j}\chi^2_{\boldsymbol{u}}$) and $\{\boldsymbol{m}^l\}$ the second member vector based on the residual fields

$$M^l_{ij} = \sum_t \sigma_i(t) b^l_n B_{nm}(t) b^l_m \sigma_j(t) \tag{16}$$

and

$$m^l_j = \sum_{\boldsymbol{r},t} \rho(\boldsymbol{r}, t, \boldsymbol{u}^{l-1}) \sigma_j(t) b^l_n S_n(\boldsymbol{r}, t) \tag{17}$$

A general overview of the 4D PGD P-DVC procedure is shown in the algorithm 1. Even though a maximum value of iterations or convergence criteria, ϵ_p and ϵ_α, can be enforced to stop the fixed-point algorithm, this revealed unnecessary as the maximum number of iterations to reach stagnation is usually quite low (*i.e.,* 3-5).

Algorithm 1 4D-P-DVC fixed-point procedure

while High residual norm **do**
  Initialize $\{\boldsymbol{a}^l\}$ and $\{\boldsymbol{b}^l\}$
  Correction $F(\boldsymbol{x}) \leftarrow F(\boldsymbol{x} - \boldsymbol{u}^{l-1})$
  Compute updated projected sensitivities $S_i(\boldsymbol{r}, t)$, Equation (10)
  while $\| \sum_{j=1}^{N_s} \Delta b^l_j \boldsymbol{\Phi}_j(\boldsymbol{x}) \| < \epsilon_p$ and $\|\Delta\{\alpha^l\}\| < \epsilon_\alpha$ **do**
    Compute spatial mode $\{\boldsymbol{b}^l\}$, Equation (12)
    Compute temporal amplitude $\{\boldsymbol{a}^l\}$, Equation (15)
  end while
  Update displacement field $\boldsymbol{u}^l$, Equation (7) $l = l + 1$
end while

3 Application to slender samples

It is proposed to analyze the kinematics of a nodular graphite cast iron dog bone sample during *in situ* tension until failure (Figure 1(a)). As many of the standard *in situ* test geometries, the proposed sample is slender and may be considered as a beam with one dimension much higher than the other two. An appropriate kinematic regularization based on a very small number of degrees of freedom is thus proposed.

3.1 Slender-shaped specimen kinematics

The slender geometry is axially divided into N_s undeformable beam sections, normal to the beam axis, with trilinear interpolations. The displacement field is hence written in this reduced basis

$$\boldsymbol{\Phi}_i(x) = \sum_{j=1}^{N_s} \sum_{k=1}^{6} p_j(z) \boldsymbol{\psi}_k(\boldsymbol{x}) \tag{18}$$

with $i = (j, k)$, $\boldsymbol{\psi}_k(\boldsymbol{x})$ the 6 rigid body motions of the entire sample, $p_j(z)$ the shape functions that allow specific sections to be selected and interpolations to be performed between them. For a linear interpolation, the shape function will be triangular functions whose maxima are located at the section positions and its length will correspond to the size of two sections. It can be noted that the shape functions are the same for all sections (thus do not depend on mode j). The consequence is some coupling between rotation and translation for the section far from the center of rotation. In the present application, the beam is composed of 15 cross-sections (see Figure 1(c) for the depiction of few sections on the slender sample used in the application), each animated with 6 Rigid Body Motions (RBMs, *i.e.,* 3 translations and 3 rotations).

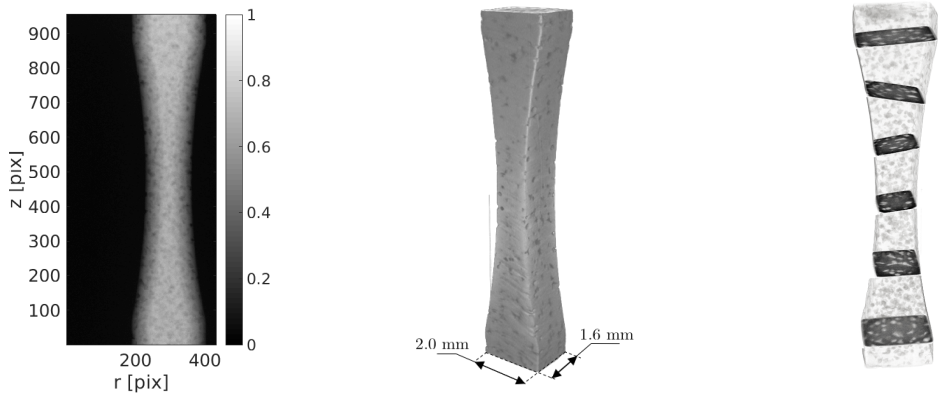

(a) (b) (c)

Figure 1: (a) Radiograph of the sample (the rotation axis is at the center of the image). Gray levels have been normalized so that the maximum log-attenuation is set to 1, and that of air to 0. (b) Reconstructed volume, and (c) the proposed space regularization with rigid body motions on few sections of the beam

3.2 Time dependence

Generically, in the time dimension, $\sigma_i(t)$ are chosen functions that also introduce temporal regularizations [38, 39]. The availability of additional measurements, such as tensile loads, $T(t)$, also offers the possibility to define temporal variations that may depend on load rather than time, or any combination that may be physically motivated. This is a very convenient and non-intrusive way of incorporating some information, or some possible relationship, in the measurement parameterization. Ultimately, no time regularization can be introduced if wanted by choosing as elementary functions $\sigma_i(t)$, functions valued 1 only for time step $t = t_i$ and 0 otherwise. Other basic examples are provided by tent shaped (piecewise linear) functions, polynomials, Fourier modes and splines.

In the treated application, the time basis does not change with mode identification thus does not depend on i, but such cases could be designed (if the goal was for example to extract first the elastic part of the test).

4 Test case

4.1 Tomography acquisitions

The application case for this study is an *in situ* tensile test on a nodular graphite cast iron sample (similar sample geometry can be found in Refs. [40, 13, 14]). The geometry of the sample is described in Figures 1(b) and 2a. The central part was thinned with a radius of 20.5 mm in order to ensure that the specimen would break in the ligament area and not in the grips. The sample was mounted in an *in situ* tensile testing machine similar to that used by Buffière *et al.* [41] (see Figure 2b) and was scanned in the LMT equipment (X-View X50-CT, North Star Imaging, 180 kV, 130 µA, W target). The voxel size (using 4×4 binning at the acquisition stage) was set to 10.7 µm.

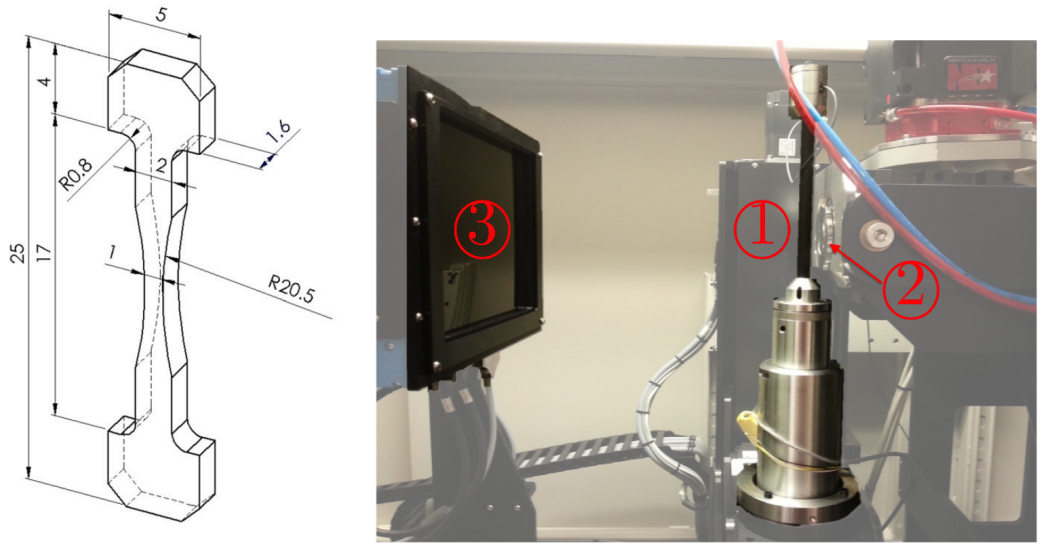

(a) (b)

Figure 2: *In situ* tensile test with (a) the dog-bone sample used in the present procedure (measured size of the rectangular cross section of 1.31×0.91 mm^2). (b) Testing setup with ① the testing machine with a carbon fiber composite loading tube, ② the X-ray source, and ③ the X-ray detector

Two flat-fields and one dark-field were acquired after conditioning and before the experiment in order to perform flat-field and dark-field corrections. Each radiograph was averaged with 5 frames in order to reduce acquisition noise without loosing too much time (it is noteworthy that a single frame would have been sufficient inasmuch as noise were white and Gaussian). The radiographs had a definition of 954×768 pixels and an initial crop of the edges allowed its size to be reduced to 954×432 pixels (Figure 1(a)). All the projections used herein have been normalized to 0 for air, and 1 for the maximum log-attenuation, after dark-field and white field corrections as well as beam-hardening corrections. In order to perform a multiscale approach, one lower scale was used in the following procedure.

Coarse graining of 2×2 elementary pixels into one superpixel was carried out with the convolution of the projections by a Gaussian kernel with a characteristic width of 2 pixels, and downsampling to a coarse 2×2 regular square grid to create smaller images (called images at scale 2). The projections were obtained after flat field normalization and standard (*i.e.,* third order polynomial) beam hardening corrections [42] due to the high absorption of the ferritic matrix. Reconstructions and projections were performed with the ASTRA toolbox [43], using the Feldkamp-Davis-Kress (FDK) procedure suited for cone beams [44]. The initial projection $f(\boldsymbol{r}, \theta)$ were compared with the re-projection of the reconstructed volume $\Pi_k[F(\boldsymbol{x})]$. The SNR of these projection residuals was 21.70 dB. These systematic reconstruction/reprojection residuals were then subtracted to the projected volume in the following procedure after a 2D registration.

4.2 In-situ tensile test

The fast space-time *in situ* experiment is composed of three phases:

1. loading to $T = 250$ N in order to remove the backlash that would introduce rigid body motions,

2. a complete scan of the reference state (at 250 N) that consisted of 600 radiographs captured at equally spaced angles ranging over a full 360° rotation. This scan took 22 min to be acquired,

3. continuous rotation of the sample with 50 projections per full rotation at a rate of one projection every 2 s. One hundred twenty seven projections were acquired during 2.5 full rotations (as illustrated in Figure 3). The first full rotation (*i.e.,* 50 time steps or 100 s) was performed at constant load and was used to quantify the uncertainty. The remaining rotation (starting after 100 s) was carried out with a continuous load change (from 250 to 750 N), as shown in Figure 4, controlled at a constant stroke velocity of 2 µm/s.

Figure 3 shows 3 selected projections at different times, angles and load. The particular choice of these angles will be discussed after the analysis of the results. The 60-pixel wide right and left edges of the radiographs and 100-pixel long top and bottom parts were discarded. This operation avoided the top and bottom parts whose quality was low because of the divergent X-ray beam and reconstruction process.

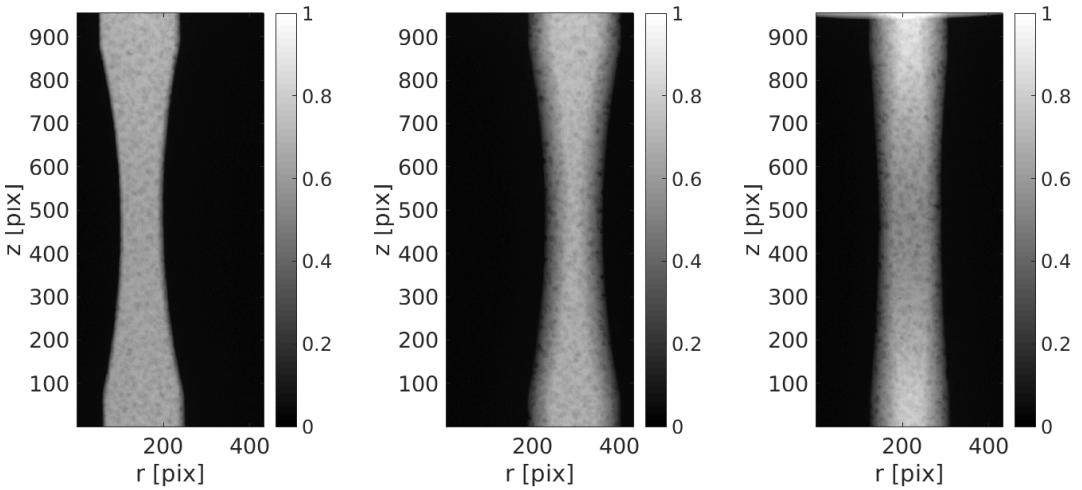

(a) (b) (c)

Figure 3: Projection at scale 1 of the sample at different angles and load during the tensile experiment. Projections are normalized between 0 (air) and 1 (maximum attenuation over a full rotation). (a) Time step 90, $\theta = 80°$, $T = 630$ N. (b) Time step 110, $\theta = -64.8°$, $T = 715$ N. (c) Time step 123, $\theta = -158.4°$, $T = 736$ N.

The measured axial force T during the test at each radiograph acquisition is shown in Figure 4. This signal is used in the work only as a component of the time basis. The force measurement will play a much stronger role for the elastoplastic identification (see the companion paper [45]).

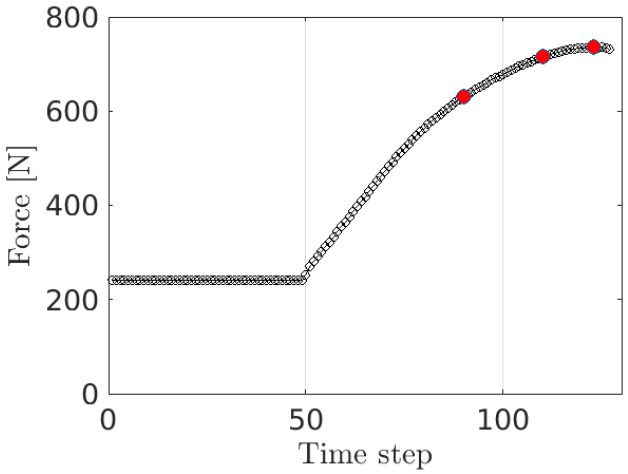

Figure 4: One hundred twenty seven force measurements $T(t)$ of the tensile test starting from 250 N. A first rotation is performed at constant load (corresponding to the first plateau until the 50th time step, or 100 s). Then the load is increased until failure. The three red dots are the projections shown in Figure 3 for time steps 90, 110 and 123.

The temporal basis used to measure the rigid body motions is composed of $N_n = 7$ time functions $\sigma_n(t)$ (Table 1). The sine and cosine functions are introduced as they are expected to occur for a slight misalignment of the sample with respect to the rotation axis [27].

Table 1: Temporal basis chosen for the kinematic measurement.

$\sigma_1(t)$	$\sigma_2(t)$	$\sigma_3(t)$	$\sigma_4(t)$	$\sigma_5(t)$	$\sigma_6(t)$	$\sigma_7(t)$
$T(t)$	$\sin(\theta(t))$	$\cos(\theta(t))$	$t^0 = 1$	t^1	$\max((t-50), 0)$	$\max((t-50), 0)^2$

The initial residual field is shown in Figure 5 for the three selected angles at different time steps and loads of the procedure with a divergent color map that highlights the positive and negative patterns (so as to ease the visual interpretation of a residual displacement). Let us stress that here and in all subsequent figures showing residuals, the gray level normalizations of the initial projections between 0 and 1 have been preserved so that the color bar values can be compared. Large levels of the residual field are observed at the edges of the sample corresponding to large rigid body motions. The initial SNR is 9.94 dB.

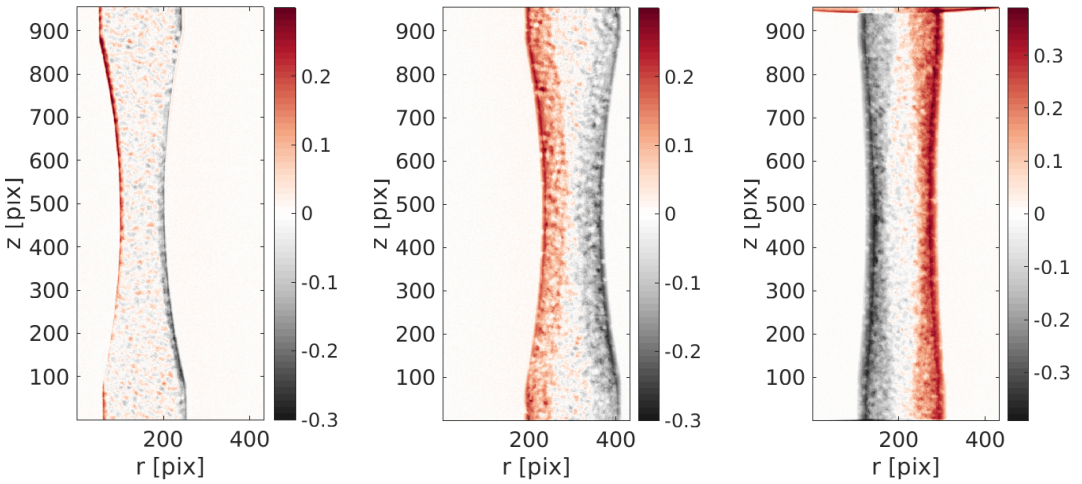

Figure 5: Initial residual field (keeping the projection normalization) composed of a large motion for (a) time step 90, $\theta = 80°$, $T = 630$ N, (b) time step 110, $\theta = -64.8°$, $T = 715$ N, (c) time step 123, $\theta = -158.4°$, $T = 736$ N.

4.3 Rigid body motion measurement

It is first convenient to start erasing the mean RBMs that occurred during the mechanical test, which are due to compensated backlash or the testing machine compliance. Instead of studying each section independently, it is proposed to use $p_j(z) = 1$. Six spatial degrees of freedom (*i.e.,* the 6 RBMs) are hence measured for each mode (*i.e.,* the three translations

and three rotations). This makes a total of 42 unknown amplitudes. The PGD approach consists in sorting out all those 42 degrees of freedom in "modes," such that the first is the "major" one, in the sense that it allows the residual to decrease by the largest amount.

Eight rigid body modes are measured at scale 2 until the root-mean-square average residual no longer decreases. Because of the successive updates of the non-linear problem (image registration) after each mode acquisition, the identified modes are not expected to be strictly orthogonal to each other. Hence, there is no reason to converge after the 6 modes that would result from the singular value decomposition of a full identification procedure. The choice of scale 2 is a matter of convenience as long as it is much cheaper computationally, and sufficient for RBM evaluations, as this is only a pre-correction. The results are then applied to scale 1. The residual fields for the three selected angles are shown in Figure 6. Note that the color scale is magnified by a factor of 4 since a large part of the initial residual has been erased. It is observed that the edges of the projection are composed of large vertical and horizontal scratches due to the registration process. Those areas are not taken into account in the SNR measurement. The SNR at this step of the procedure is 25.4 dB confirming this observation.

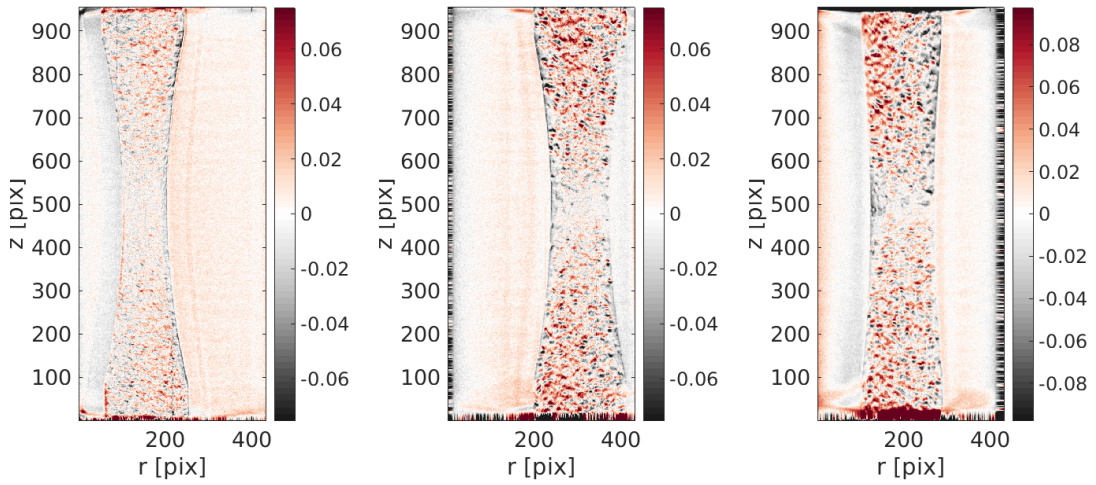

Figure 6: Residual field after the rigid body motion correction. Tensile patterns not yet corrected are visible at (a) time step 90, $\theta = 80°$, $T = 630$ N, (b) time step 110, $\theta = -64.8°$, $T = 715$ N, (c) time step 123, $\theta = -158.4°$, $T = 736$ N.

What is visible from these images is that the central part has been properly corrected by the rigid body motions. The top and bottom parts are composed of moving features that will be corrected by the next procedure. The mean translation values are shown in Figure 7, and designated as $\langle u_x \rangle$, $\langle u_y \rangle$ and $\langle u_z \rangle$. The vertical $\langle u_z \rangle$ component evolves with the applied force and corresponds to the compliance of the testing machine, and the motion of the bottom part of the sample by the grip. The $\langle u_x \rangle$ component is a transverse motion between the rotation axis and the sample, which accidentally almost coincides with the

x-axis as can be seen from the fact that $\langle u_y \rangle$ is much smaller.

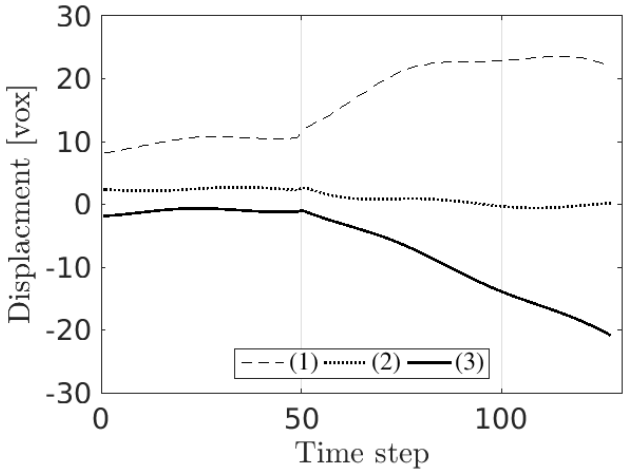

Figure 7: Mean corrected translation measured with 8 rigid body motion modes for all loading steps with (1), (2) and (3) respectively corresponding to $\langle u_x \rangle$, $\langle u_y \rangle$ and $\langle u_z \rangle$.

4.4 Tensile deformations

From the previous corrected residual fields where the rigid body motions have been erased, it is now possible to measure motions corresponding to a tensile deformation. Each section of the beam is now considered as being independent. 4 deformation modes are measured (for a problem composed of 630 degrees of freedom). The residual field at the end of the procedure is shown in Figure 8 and reaches a mean SNR value of 26.7 dB.

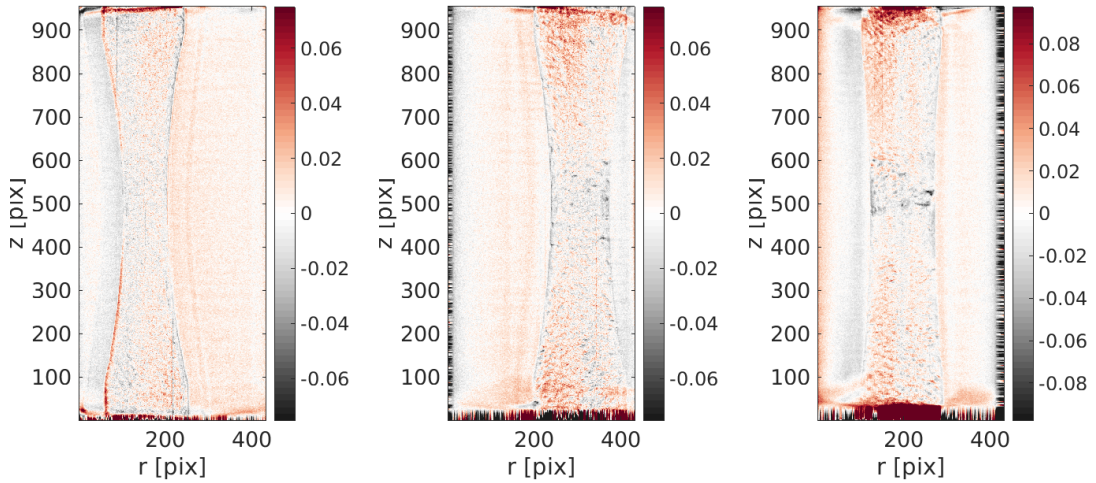

Figure 8: Residual field at the end of the procedure. (a) Time step 90, $\theta = 80°$, $T = 630$ N, (b) time step 110, $\theta = -64.8°$, $T = 715$ N, (c) time step 123, $\theta = -158.4°$, $T = 736$ N.

It is observed that the previous alternating positive and negative features have disappeared. The captured displacement field correctly reduces the residual and thus is deemed trustworthy. Some residuals are still visible in the center of the sample and may be a consequence of the shrinkage of the section expected from plastic incompressibility, but not included in the chosen kinematics. The dark residual located in the central part for the last steps (see Figure 8c) is due to localized necking, a precursor to ductile fracture that will break the sample shortly thereafter, at step 127.

The initial SNR for each step is shown in Figure 9. The time periodicity that is seen on the graph, with a period of 25, is due to specific angles at which the residuals are more sensitive to the displacement field (e.g., angles where the faces of the sample are parallel to the X-ray beam). The significant improvement from the initial images shows the accuracy of the proposed 4D approach. Step 50 has an accidentally low SNR value and corresponds to the beginning of the load variation.

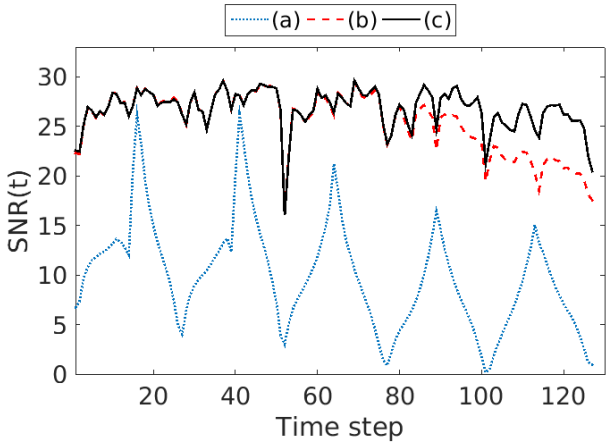

Figure 9: SNR of each projected residual field. The mean value, 9.9 dB for the initial SNR (a), 25.4 dB for the RBM corrected (b) and 26.6 dB for the corrected residual (c) shows an excellent description of the kinematics.

The vertical displacement field and the vertical strain $\varepsilon_{zz} = \partial_z u_z(t)$ for each section is shown in Figure 10. The mean tensile extension between the top and bottom part reaches about 15 voxels. A large plastic strain concentration (*i.e.,* not only proportional to the force measurement) is visible in the central part as expected from the chosen geometry.

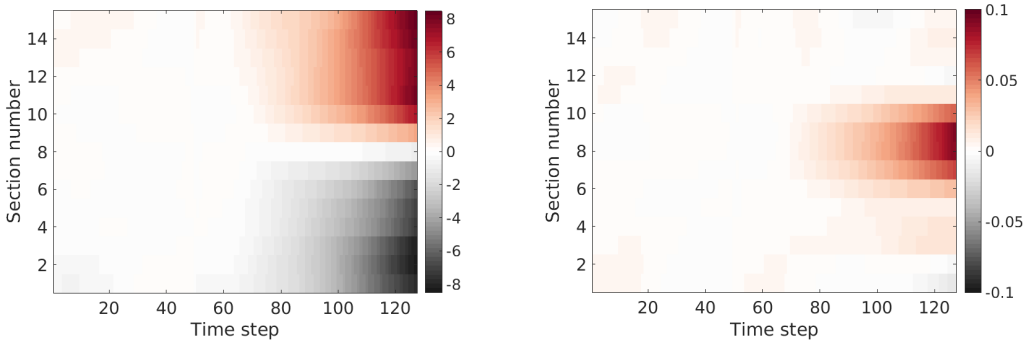

(a) $\langle u_z(z,t)\rangle_{(x,y)}$ (b) $\langle \varepsilon_{zz}(z,t)\rangle_{(x,y)}$

Figure 10: (a) Measured vertical displacement field for each sections without rigid body motions, expressed in voxels, and (b) corresponding vertical strain. A large strained zone of approximately $8-9\%$ appears in the central part.

The very small displacement field in the first part [0;50] should be null. However it cannot be considered as uncertainty because some real displacements due to creep for example could appear. It can also be noted that the strain field displays some heterogeneities (see *e.g.,* Section 4 at the end of the experiment) that was not anticipated from the geometry. Adding some regularizations (*e.g.,* local mechanical regularization or directly from models) would provide a smoother field.

5 Discussion

5.1 Kinematics

The kinematics was simplified in the spirit of that used in beam theory (*i.e.,* slender body). The displacement field was assumed to be well approximated by a rigid body motion for each section of the sample, but these rigid body motions were slowly varying along the longitudinal axis. This assumption is quite generic and believed to be applicable to many uniaxial mechanical tests. In the present study, six parameters (*i.e.,* three translations and three rotations) for each rigid body motion defined at 15 cross-sections were linearly interpolated along the sample axis. Hence 90 kinematic parameters defined the motion at each instant of time. Seven time functions were introduced to account for the loading history, namely, a discretization involving a total of 630 kinematic degrees of freedom to be determined.

The choice of such a discretization is, by itself, a regularization. It was here designed to suit a slender body loaded along its longitudinal axis. However, for other cases, additional degrees of freedom may be introduced. Any information about the experiment may be used to regularize the displacement field and find a 'smart' 4D-kinematic basis, *e.g.,* crack propagation, sudden motion (because of a shock), temperature variations. The number of unknowns may not be the major limitation of the method when a PGD procedure is used, yet including part of prior knowledge in a relevant kinematics is always beneficial. With

such a suited parameterization of the kinematics, the approach followed in the present study can be generalized without notable restrictions. The only requirement is to keep the evolution between consecutive radiographs progressive and that during the experiment, the rotation has been large enough (a few full 360° rotations is appropriate), otherwise uncertainty may be large in some directions.

5.2 PGD

The proposed methodology relied on model order reduction, namely, PGD. By itself, PGD is not restrictive (*i.e.,* separated form for the time and space variations is not limiting) nor does it rely on any smoothness assumption. It is meant to exploit the intrinsic "simplicity" of the problem, which is however difficult to formulate in other terms than saying that only few "modes" are needed for describing the kinematics. Additionally, this number of modes is not a priori defined. Rather, being driven to lower the residuals, one may argue that PGD is a smart technique able to pick up only those degrees of freedom, or modes, that are relevant, hence making the algorithm very efficient but not intrinsically based on smoothness. It has been shown that smoothness could independently be tuned through regularization [45].

In the present case, instead of an exhaustive analysis of all 630 degrees of freedom, PGD was used to select the relevant modes. Convergence was considered satisfactory based on residuals after 8 rigid body modes and 4 deformation modes. Thus the efficiency of this model reduction technique is very significant. Let us stress that a space and time separation accounting for the deformation of samples is quite generic and is expected to have a very broad range of applicability with a similar high level of efficiency.

5.3 Residuals

The residual field (*i.e.,* differences at all angles between the projected and corrected volume and the deformed radiographs) that were minimized are the key information to validate the method. It gives a global and quantitative evaluation of the trustworthiness of the results and — if and where relevant — allows error areas (due to noise, imperfect convergence, sensor artifacts or model errors) to be visually localized and interpreted. In the present case, it was observed that the residuals mostly showed imperfections of the X-ray detector. From this observation, it was earlier suggested that the choice made prior to the experiment of averaging over 5 frames each radiography could have been reduced presumably to a single acquisition. Let us also note that the last residuals show localized features than can be interpreted as the inception of a crack. This observation stresses once more the value of such residual fields.

Additionally, residuals can also be quantified in terms of Signal-to-Noise Ratio (SNR). In the reported example, the mean SNR of the residual fields increased from 9 dB to 26.6 dB along with the correction by the 4D displacement field. This residual change highlights the accuracy of the results. The measured displacement field was presented for the vertical component (although all other components were captured). A tensile

displacement amplitude of 15 voxels was measured at the end of the experiment and high strain levels were concentrated in the central part of the specimen, as expected from its geometry, until localization leads to ductile failure.

6 Conclusion

The full 4D (*i.e.,* 3D space and time) kinematics of the 6 min experiment was captured with an extension of P-DVC that uses a model order reduction technique (PGD). Based on regularized fields relying on the slender sample geometry as well as a dense sampling in time, this method measures displacement fields from single projections at each time (or load) step of the experiment instead of reconstructed volumes in standard DVC methods.

The procedure was tested with an *in situ* tensile test on nodular graphite cast iron composed of 127 radiographs with continuous load changes and rotation of the sample until failure. The experiment was carried out in a lab tomograph with an X-ray cone beam source. The entire experiment was carried out in 300 s, which is more than two orders of magnitude faster than standard methods. This performance goes together with the benefit of having a continuous (*i.e.,* uninterrupted) loading so that load and rotation can be varied simultaneously. PGD was used to only focus on important space and time separated modes, thereby reducing the number of effective kinematic degrees of freedom, not from prior judgment, but as called by the experiment itself.

The measurement of the kinematics is a first step toward mechanical identification, which is one of the major goals of experimental mechanics [46]. Being able to measure the 4D motions of the studied sample at fast rates is a major asset. From the estimated displacement fields at each space and time steps, it is possible to use an inverse method in order to calibrate the mechanical parameters of, say, an elastoplastic model. Another variant called "integrated measurement" directly identifies the model parameters from the images, here radiographs, and is presented in a companion paper [45].

Acknowledgement

This work has benefited from the support of the French "Agence Nationale de la Recherche" through the "Investissements d'avenir" Program under the reference ANR-10-EQPX-37 MATMECA and ANR-14-CE07-0034-02 COMINSIDE.

References

[1] E. Maire. On the application of X-ray microtomography in the field of materials science. *Advanced Engineering Materials*, 3(8):539–546, 2001.

[2] L. Salvo, P. Cloetens, E. Maire, S. Zabler, J.J. Blandin, J.Y. Buffière, W. Ludwig, E. Boller, D. Bellet, and C. Josserond. X-ray micro-tomography an attractive charac-

terisation technique in materials science. *Nuclear instruments and methods in physics research section B: Beam interactions with materials and atoms*, 200:273–286, 2003.

[3] J. Desrues, G. Viggiani, and P. Bésuelle, editors. *Advances in X-ray Tomography for Geomaterials*. Wiley / ISTE, London (UK), 2006.

[4] L. Salvo, M. Suéry, A. Marmottant, N. Limodin, and D. Bernard. 3D imaging in material science: Application of X-ray tomography. *Comptes Rendus Physique*, 11(9):641–649, 2010.

[5] E. Maire, C. Le Bourlot, J. Adrien, A. Mortensen, and R. Mokso. 20 Hz X-ray tomography during an in situ tensile test. *International Journal of Fracture*, 200(1):3–12, 2016.

[6] J. Desrues, R. Chambon, M. Mokni, and F. Mazerolle. Void ratio evolution inside shear bands in triaxial sand specimens studied by computed tomography. *Géotechnique*, 46(3):529–546, 1996.

[7] A. Guvenilir, T.M. Breunig, J.H. Kinney, and S.R. Stock. Direct observation of crack opening as a function of applied load in the interior of a notched tensile sample of AlLi 2090. *Acta Materialia*, 45(5):1977–1987, 1997.

[8] F. Beckmann, R. Grupp, A. Haibel, M. Huppmann, M. Nöthe, A. Pyzalla, W. Reimers, A. Schreyer, and R. Zettler. In-Situ Synchrotron X-Ray Microtomography Studies of Microstructure and Damage Evolution in Engineering Materials. *Advanced Engineering Materials*, 9(11):939–950, 2007.

[9] E. Maire and P.J. Withers. Quantitative X-ray tomography. *International Materials Reviews*, 59(1):1–43, 2014.

[10] M. Mostafavi, D.M. Collins, B. Cai, R. Bradley, R.C. Atwood, C. Reinhard, X. Jiang, M. Galano, P.D. Lee, and T.J. Marrow. Yield behavior beneath hardness indentations in ductile metals, measured by three-dimensional computed X-ray tomography and digital volume correlation. *Acta Materialia*, 82:468–482, 2015.

[11] B. Rahmani, E. Ghossein, I. Villemure, and M. Levesque. In-situ mechanical properties identification of 3D particulate composites using the Virtual Fields Method. *International Journal of Solids And Structures*, 51(18):3076–3086, 2014.

[12] A. Bouterf, J. Adrien, E. Maire, X. Brajer, F. Hild, and S. Roux. Failure Mechanisms of Plasterboard in Nail Pull Test Determined by X-ray Microtomography and Digital Volume Correlation. *Experimental Mechanics*, 56:1427–1437, 2016.

[13] F. Hild, A. Bouterf, L. Chamoin, H. Leclerc, F. Mathieu, J. Neggers, F. Pled, Z. Tomičević, and S. Roux. Toward 4D Mechanical Correlation. *Advanced Modeling and Simulation in Engineering Sciences*, 3(1):26, 2016.

[14] A. Buljac, V.-M. Trejo Navas, M. Shakoor, A. Bouterf, J. Neggers, M. Bernacki, P.-O. Bouchard, T.F. Morgeneyer, and F. Hild. On the calibration of elastoplastic parameters at the microscale via x-ray microtomography and digital volume correlation for the simulation of ductile damage. *European Journal of Mechanics - A/Solids*, 72:287–297, 2018.

[15] H. Zhang, H. Toda, P.C. Qu, Y. Sakaguchi, M. Kobayashi, K. Uesugi, and Y. Suzuki. Three-dimensional fatigue crack growth behavior in an aluminum alloy investigated with in situ high-resolution synchrotron X-ray microtomography. *Acta Materialia*, 57(11):3287–3300, 2009.

[16] H. Toda, E. Maire, S. Yamauchi, H. Tsuruta, T. Hiramatsu, and M. Kobayashi. In situ observation of ductile fracture using X-ray tomography technique. *Acta Materialia*, 59(5):1995–2008, 2011.

[17] H. Leclerc, S. Roux, and F. Hild. Projection savings in CT-based digital volume correlation. *Experimental Mechanics*, 55(1):275–287, 2015.

[18] M. H. Khalili, S. Brisard, M. Bornert, Aimedieu P., J.-M. Pereira, and J.-N. Roux. Discrete digital projections correlation: a reconstruction-free Method to quantify local kinematics in granular media by X-ray tomography. *Experimental Mechanics*, pages 1–12, 2017.

[19] T. Taillandier-Thomas, C. Jailin, S. Roux, and F. Hild. Measurement of 3D displacement fields from few tomographic projections. In *Proc. SPIE 9896, Optics, Photonics and Digital Technologies for Imaging Applications IV*, volume 9896OL (DOI: 10.1117/12.2227904). International Society for Optics and Photonics, 2016.

[20] T. Taillandier-Thomas, S. Roux, and F. Hild. A soft route toward 4D tomography. *Physical Review Letters*, 117(2):025501, 2016.

[21] C. Jailin, A. Bouterf, M. Poncelet, and S. Roux. In situ μ CT-scan Mechanical Tests: Fast 4D Mechanical Identification. *Experimental Mechanics*, 57(8):1327–1340, 2017.

[22] F. Chinesta, A. Ammar, and E. Cueto. Recent advances and new challenges in the use of the proper generalized decomposition for solving multidimensional models. *Archives of Computational Methods in Engineering*, 17(4):327–350, 2010.

[23] P. Ladevèze. *Nonlinear computational structural mechanics: new approaches and non-incremental methods of calculation.* Springer Science & Business Media, 2012.

[24] M. Vitse. *Model-order reduction for the parametric analysis of damage in reinforced concrete structures.* PhD thesis, Université Paris-Saclay, 2016.

[25] J.C. Passieux and J.N. Périé. High resolution digital image correlation using proper generalized decomposition: PGD-DIC. *International Journal for Numerical Methods in Engineering*, 92(6):531–550, 2012.

[26] L.A. Gomes Perini, J.C. Passieux, and J.N. Périé. A Multigrid PGD-based Algorithm for Volumetric Displacement Fields Measurements. *Strain*, 50(4):355–367, 2014.

[27] C. Jailin, A. Buljac, A. Bouterf, M. Poncelet, F. Hild, and S. Roux. Self-calibration for lab-μCT using space-time regularized projection-based DVC and model reduction. *Measurement Science and Technology*, 29:024003, 2018.

[28] C. Jailin, M. Etxegarai, E. Tudisco, S.H. Hall, and S. Roux. Fast tracking of imbibition using time-resolved neutron tomography. *Submitted for publication*, 2017.

[29] A. Buljac, C. Jailin, A. Mendoza, J. Neggers, T. Taillandier-Thomas, A. Bouterf, B. Smaniotto, F. Hild, and S. Roux. Digital volume correlation: Review of progress and challenges. *Experimental Mechanics*, 58(5):661–708, 2018.

[30] Don H Johnson. Signal-to-noise ratio. *Scholarpedia*, 1(12):2088, 2006.

[31] S. Roux, F. Hild, P. Viot, and D. Bernard. Three-dimensional image correlation from X-ray computed tomography of solid foam. *Composites Part A: Applied science and manufacturing*, 39(8):1253–1265, 2008.

[32] H. Leclerc, J.-N. Périé, S. Roux, and F. Hild. Voxel-scale digital volume correlation. *Experimental Mechanics*, 51(4):479–490, 2011.

[33] J. Lachambre, J. Réthoré, Arnaud Weck, and Jean-Yves Buffière. Extraction of stress intensity factors for 3d small fatigue cracks using digital volume correlation and x-ray tomography. *International Journal of Fatigue*, 71:3–10, 2015.

[34] T. Taillandier-Thomas, S. Roux, T.F. Morgeneyer, and F. Hild. Localized strain field measurement on laminography data with mechanical regularization. *Nuclear Instruments and Methods in Physics Research Section B: Beam Interactions with Materials and Atoms*, 324:70–79, 2014.

[35] A. Bouterf, S. Roux, F. Hild, J. Adrien, E. Maire, and S. Meille. Digital Volume Correlation Applied to X-ray Tomography Images from Spherical Indentation Tests on Lightweight Gypsum. *Strain*, 50(5):444–453, 2014.

[36] A. Nouy. A priori model reduction through proper generalized decomposition for solving time-dependent partial differential equations. *Computer Methods in Applied Mechanics and Engineering*, 199(23):1603–1626, 2010.

[37] T.H. Cormen. *Introduction to algorithms*. MIT press, 3rd edition, 2009.

[38] G. Besnard, S. Guérard, S. Roux, and F. Hild. A space–time approach in digital image correlation: Movie-DIC. *Optics and Lasers in Engineering*, 49(1):71–81, 2011.

[39] G. Besnard, H. Leclerc, F. Hild, S. Roux, and N. Swiergiel. Analysis of Image Series through Digital Image Correlation. *J. Strain Analysis*, 47(4):214–228, 2012.

[40] Zvonimir Tomičević, Janoš Kodvanj, and François Hild. Characterization of the nonlinear behavior of nodular graphite cast iron via inverse identification–analysis of uniaxial tests. *European Journal of Mechanics-A/Solids*, 59:140–154, 2016.

[41] J.-Y. Buffière, E. Maire, J. Adrien, J.-P. Masse, and E. Boller. In situ experiments with X ray tomography: an attractive tool for experimental mechanics. *Experimental mechanics*, 50(3):289–305, 2010.

[42] G.T. Herman. Correction for beam hardening in computed tomography. *Physics in medicine and biology*, 24(1):81, 1979.

[43] W. Van Aarle, W.J. Palenstijn, J. De Beenhouwer, T. Altantzis, S. Bals, K.J. Batenburg, and J. Sijbers. The ASTRA Toolbox: A platform for advanced algorithm development in electron tomography. *Ultramicroscopy*, 157:35–47, 2015.

[44] L.A. Feldkamp, L.C. Davis, and J.W. Kress. Practical cone-beam algorithm. *JOSA A*, 1(6):612–619, 1984.

[45] C. Jailin, A. Buljac, A. Bouterf, F. Hild, and S. Roux. Fast 4D tensile test monitored via X-CT: Elastoplastic identification from radiographs. *Submitted for publication.*

[46] M. Grédiac and F. Hild, editors. *Full-Field Measurements and Identification in Solid Mechanics.* ISTE / Wiley, London (UK), 2012.